PROCESSING AND PROPERTIES OF MAGNESIUM-BASED COMPOSITES REINFORCED WITH LOW LEVELS OF Al_2O_3

Payam Emadi, Bernoulli Andilab and Comondore Ravindran
Centre for Near-Net-Shape Processing of Materials, Ryerson University, 350 Victoria Street, Toronto, ON M5B 2K3, Canada

https://doi.org/10.1007/s40962-021-00738-w

Abstract

Lightweight structural metals such as magnesium are gaining extensive interest due to the increasing global demand for reducing greenhouse gas emissions. In order to promote the use of magnesium, its mechanical properties must be improved. Reinforcement with hard ceramic particles is an effective means for improving the properties of Mg alloys. The current study examined the effect of 1 μm α-Al_2O_3 particles on the microstructure and mechanical properties of AZ91E Mg alloy using permanent mold stir casting. The results were evaluated through optical microscopy, scanning electron microscopy and tensile testing. Experimentally obtained tensile results were compared to theoretical strengthening mechanism models. The findings suggested that the addition of Al_2O_3 led to improvements in both microstructure and tensile properties. Through the addition of 1 wt% Al_2O_3, the grain size and yield strength improved by 61% and 11%, respectively. The highest levels of improvement for ultimate tensile strength and ductility, achieved through 0.5 wt% Al_2O_3 addition, were 15% and 79%, respectively. In addition, refinement of the alloy secondary phases was also observed. These findings were attributed to a combination of grain refinement and coefficient of thermal expansion mismatch between the matrix and the reinforcement particles. As well, the experimental results were in good agreement with the theoretical models sometimes affected by agglomeration of particles. This research demonstrated that the addition of Al_2O_3 resulted in a novel and effective method for improving the properties of Mg alloys for use in consumer electronics, aerospace applications and the transportation sector.

Keywords: *grain refinement, casting and solidification, magnesium, optical microscopy, scanning electron microscopy, mechanical properties*

Introduction

Magnesium (Mg) has been recognized as being the lightest structural metal available. It has a high strength-to-weight ratio, making it an attractive choice for applications where weight savings is a priority.[1,2] Due to the continually rising demand of the consumer electronics, aerospace and automotive industries for light weighting of components, Mg has been gaining increasing popularity. However, in order for Mg alloys to become suitable candidates for replacing aluminum- and iron-based alloys, their mechanical properties must be improved.

Improvement in mechanical properties of Mg can be achieved through the reinforcement of alloys with hard ceramic particles, producing metal matrix composites (MMC).[3–10] However, several criteria must be met to ensure the casting of an effective MMC. For example, the added ceramic particles must be carefully selected, ensuring stability in the liquid metal, crystallographic similarity between the particles and the host metal, as well as similar density to avoid rapid settling or inadvertent removal as dross.[11,12] Additionally, homogenous distribution of reinforcement particles in the alloy matrix must be attained to avoid premature failure. Therefore, particle reinforcement of Mg alloys has been the subject of much research.

Ganguly et al.[13] examined the effects of 50 nm SiC particles on the mechanical properties of an AZ91–Ca–Sb alloy prepared through squeeze casting. The researchers

Received: 04 October 2021 / Accepted: 04 December 2021 / Published online: 7 January 2022

observed improvements in ultimate tensile strength (UTS), yield strength (YS) and elastic modulus with the incorporation of SiC. Moreover, the 2 wt% SiC addition level resulted in the most improved mechanical properties. Ganguly et al.[13] attributed the improvements in properties to reduction in grain size, increase in dislocation density, Orowan strengthening and the presence of a relatively high amount of Al_2Ca in the composites.

Aydin et al.[14] studied the effect of 40–45 μm TiB_2 particle content on the mechanical behavior of AZ91 Mg alloy. The researchers prepared the metal matrix composites through powder metallurgy using hot pressing at 525 °C and 45 MPa. Uniform distribution of reinforcement particles was reported, with partial agglomeration at higher addition levels (30 wt%). In addition, the hardness of the composites showed signs of improvement with increasing TiB_2 content. Aydin et al.[14] attributed the improvement in mechanical properties to the generation of geometrically necessary dislocations through coefficient of thermal expansion mismatch between the particles and the matrix, as well as load sharing from the Mg matrix to the harder TiB_2 particles.

Recent research conducted by Nie et al.[15] analyzed TiC particle-reinforced Mg–Zn–Ca-based composites. In their study, the experimental procedure consisted of 50 nm TiC particle addition, multi-directional forging and subsequent extrusion. The researchers reported a significant improvement in strength and ductility with the addition of 0.5 wt% TiC. The improvement in mechanical properties was attributed to grain recrystallization and Orowan strengthening through precipitated $MgZn_2$ secondary phases.

In most cases, to ensure adequate distribution of reinforcement particles in the alloy matrix, complex preparation techniques such as friction stir processing, multi-directional forging or spark plasma sintering are utilized.[14–16] These fabrication techniques are typically not feasible in a high-volume production setting, since they require expensive and unique equipment. In addition, using nano-sized reinforcement particles is not viable due to their cost and difficulty in implementation. As a result, there is ongoing research to identify a cost-effective and easily implementable solution for preparing Mg-based MMCs that can be readily adapted to high-volume production settings.

In the present study, Al_2O_3 was selected as a reinforcement particle due to its high melting point relative to Mg, high strength, high density and low cost.[17–20] As well, the large coefficient of thermal expansion (CTE) mismatch between Al_2O_3 (8.2×10^{-6} °C^{-1}[21]) and AZ91 (26.2×10^{-6} °C^{-1}[22]) can promote increased CTE mismatch strengthening. Other polymorphs of Al_2O_3, such as γ-Al_2O_3, were neglected due to their instability at elevated temperatures.[23] The effect of 0.25–2 wt% addition of 1 μm α-Al_2O_3 particles on the microstructure and mechanical properties of AZ91E Mg alloy was investigated. The particle size of 1 μm was chosen to closely match heterogeneous nuclei size reported for Mg alloys and to maximize the contribution of strengthening mechanisms.[24] The experimental procedure utilized permanent mold stir casting, which can be implemented with ease in an industrial production setting. Extensive microscopy and tensile testing were carried out. Subsequently, the experimental results were related to results from theoretical strengthening mechanism models. This enabled a novel and in-depth understanding of the effects of 1 μm Al_2O_3 particle reinforcement on AZ91E Mg alloy prepared through stir casting. Such a study, incorporating the AZ91E alloy, stir casting with 1 μm α-Al_2O_3 particles, extensive optical and scanning microscopy, tensile testing and theoretical strengthening mechanism analysis, has not been performed to date.

Materials and Methods

Cast samples were prepared by melting 1 kg of AZ91E alloy ingots in an electric resistance furnace. The crucible used for melting and casting was composed of low carbon steel with a diameter of 110 mm and a height of 150 mm. The furnace temperature was set to 750 °C, and an atmosphere of 4.7 L/min of CO_2 and 0.5 vol% SF_6 was used to prevent oxidation.[25] Once the ingots were molten, the surface of the melt was skimmed of dross and subsequently poured into an ASTM B 108-6 permanent standard tensile mold coated with SFP Micawash No. 15 refractory coating.[26] The pouring temperature of the melt was 720 °C, and the mold was pre-heated to 350 °C to enable a controlled cooling rate. The result of each casting was two standard round tensile bars. The chemical composition of the alloy measured using an Oxford Instruments optical emission spectrometer (Foundry Master Pro) can be seen in Table 1.

The composites were prepared using 1 μm α-Al_2O_3 particles with 99.99% purity. Prior to casting, the particles were pre-heated to 200 °C for removal of moisture. Addition levels of 0.25, 0.5, 1 and 2 wt% were utilized. Once the melt temperature reached 740 °C, the surface was skimmed, and the Al_2O_3 particles were added. The particles were contained in an aluminum foil to facilitate their addition. Subsequently, the melt was stirred for 3 min at 300 rpm using a low carbon steel pitched blade impeller with rounded blades. The diameter of the impeller was 60

Table 1. Average Chemical Composition of the AZ91E Ingots (wt%)

Al	Mn	Zn	Si	Fe	Cu	Mg
8.94	0.21	0.68	0.0075	0.0031	< 0.002	Balance

mm with three equally spaced blades and a pitch of 45°. The impeller was immersed to a depth of 20 mm from the bottom of the crucible. For each condition, including the base alloy, two casting trials were carried out, producing four tensile bars.

Tensile testing was performed using a United Universal Testing Machine (Model STM-50kN) according to ASTM B 557M-15.[27] The tests were performed at ambient temperature using a pull rate of 12.5 mm/min. The ductility of the samples was determined using an extensometer during testing. For metallographic analysis, sections were extracted from the tensile bar gauge area, 10 mm from the fracture surface. The samples were ground using SiC paper and polished with 9, 3 and 1 μm oil-based diamond suspension.

Microstructural analysis and secondary phase identification were performed using a JEOL scanning electron microscope (SEM) (Model 6380LV) equipped with an energy-dispersive X-ray spectrometer (EDS). For grain size analysis, a Nikon Eclipse metallurgical microscope (Model MA200) was used. Prior to measurement, samples were solution heat treated according to ASTM B661-12 and etched using a 95% distilled water and 5% citric acid solution, revealing grain boundaries.[28] For each casting condition, a total of 20 images captured at 100 × magnification were measured using the linear intercept procedure specified in ASTM E 112-13.[29]

Results

Grain Size Analysis

Figure 1a displays an optical micrograph of the base AZ91E alloy. The image was captured post-solution heat treatment at 413 °C for 24 h and etching using a distilled water and citric acid solution, to clearly display the grain boundaries. The base alloy contained a coarse grain structure with irregular grain boundaries. With the addition of 0.25 wt% Al_2O_3, the grain size displayed signs of refinement, as shown in Figure 1b. In particular, the average grain diameter appeared to be smaller, and the grain boundaries were more laminar. However, the grain structure was not wholly uniform, and a variation of both fine and coarse grains was present. Improvements in the grain size, shape and uniformity were observed with increasing Al_2O_3 content. In effect, the microstructure of the alloys displayed gradual enhancement up to 1 wt% Al_2O_3. However, no discernable changes in the grain structure were observed by increasing the refiner content from 1 to 2 wt% Al_2O_3.

The average grain diameter for the base AZ91E castings and the samples refined with Al_2O_3 is summarized in Figure 2. All measurements were performed on solution heat treated and etched samples. Using the linear intercept method, the grain diameter of the base alloy was determined to be 202 μm. The addition of Al_2O_3 improved the average grain size of the alloys. With the addition of 0.25 wt% Al_2O_3, the average grain size decreased to approximately 125 μm. This marked a decrease in grain size of 38%. Further Al_2O_3 particle addition to 0.5 wt% and 1 wt% decreased the average grain size of the alloys to approximately 100 μm and 79 μm, respectively. However, further increasing the Al_2O_3 weight fraction to 2 wt% did not continue to improve the alloy grain size. As a result, the greatest improvement in average grain size was observed for the 1 wt% addition level, which led to a 61% reduction in average grain diameter.

Microstructural Analysis

The microstructure of the as-cast base AZ91E alloy is presented in Figure 3a. The alloy microstructure consisted of the α-Mg matrix, β-$Mg_{17}Al_{12}$ eutectic phases and Al–Mn-based intermetallics. Energy-dispersive X-ray spectroscopy results confirming the presence of these phases can be seen in Figure 3b–d, respectively. The β-$Mg_{17}Al_{12}$ phase typically precipitates on grain boundaries.[25,30] The morphology of this phase is in the form of coarse and large networks. Further, the eutectic phase is the last phase to form during solidification.[25] In contrast, the Al–Mn-based intermetallics are the first phase to precipitate during solidification.[25] The intermetallics are present in two forms, needle-like or blocky, and they are mostly found in clusters within the Mg matrix. In the absence of a more potent nucleant, the Al–Mn phases have been reported to act as nucleation sites for α-Mg.[31]

Figure 4 displays the microstructure of the AZ91E alloy with the addition of 0.25 wt% Al_2O_3. Similar to the base alloy, the microstructure consisted of the Mg matrix, the β-$Mg_{17}Al_{12}$ eutectic phases and Al–Mn-based intermetallics. The β-$Mg_{17}Al_{12}$ networks appeared shorter and smaller in size relative to those observed in the base alloy, which is a direct result of the finer grain size of the reinforced alloy. No significant changes were observed in the morphology or distribution of the Mn–Al-based intermetallics. Further, the figures also displayed particles of Al_2O_3 within the microstructure as shown in Figure 4c, with the associated EDS spectrum in Figure 4d. The particles appeared to be well distributed throughout the microstructure, with no signs of agglomeration. Particles were also observed near the center of grains alongside the Mn–Al phase, which may indicate that they were a source for nucleation of α-Mg.

Scanning electron micrographs of the alloy refined with 0.5 wt% Al_2O_3 can be seen in Figure 5. At this addition level, the β-$Mg_{17}Al_{12}$ networks appeared significantly smaller and shorter in length as compared to the base alloy. Again, this was thought to be a result of the finer grain size. The

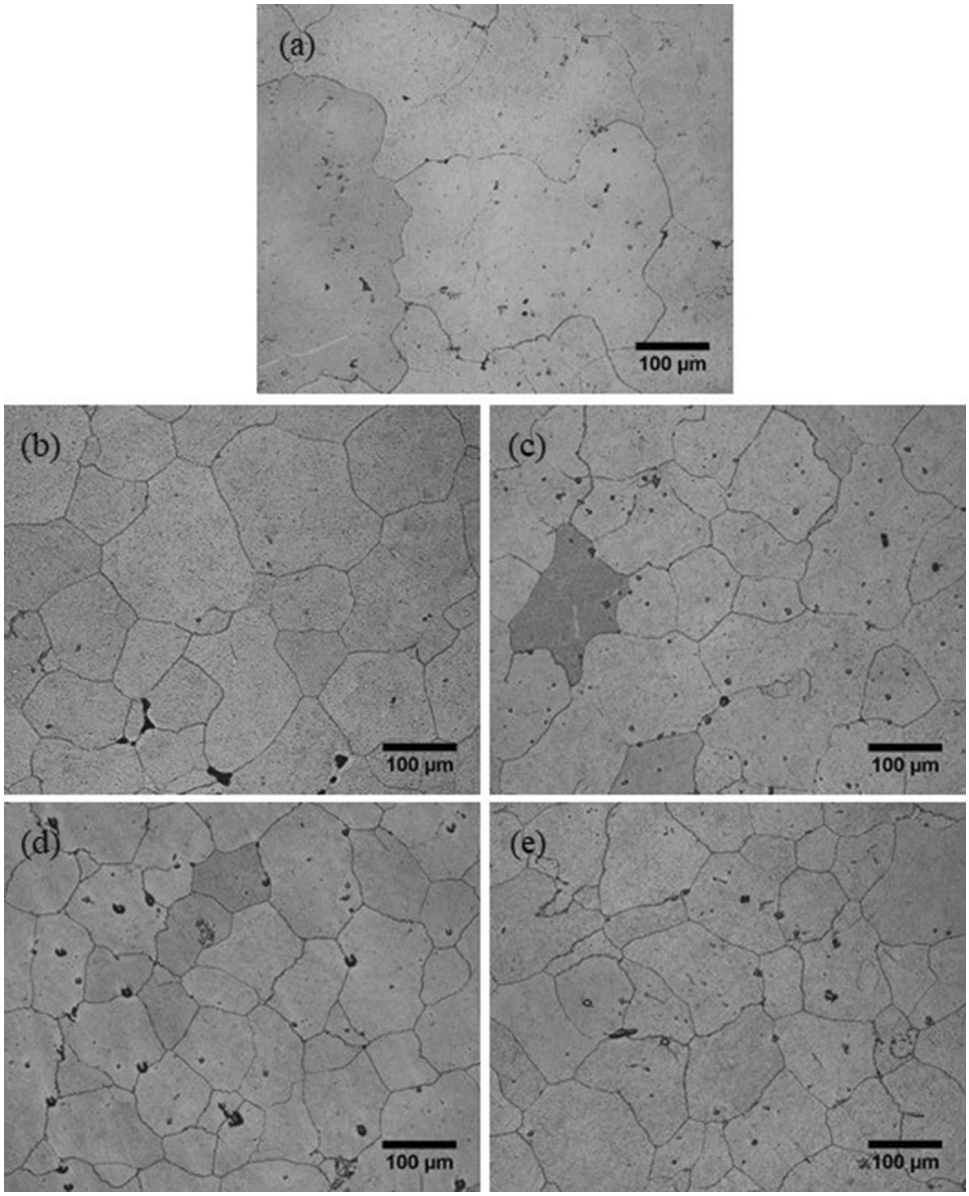

Figure 1. Optical micrographs, captured post-heat treatment and etching, displaying the typical grain structure of (a) AZ91E base alloy, (b) AZ91E + 0.25 wt% Al_2O_3, (c) AZ91E + 0.5 wt% Al_2O_3, (d) AZ91E + 1 wt% Al_2O_3 and (e) AZ91E + 2 wt% Al_2O_3.

shape of the Mn–Al-based intermetallics was also modified. Flower-like morphologies of the intermetallics were observed near Al_2O_3 particles, as depicted in Figure 5b. The distribution of the Al_2O_3 particles within the matrix was less uniform when compared to the 0.25 wt% Al_2O_3 condition. As mentioned, small clusters of Al_2O_3 were observed near the Mn–Al intermetallics, which may have prompted their altered shape (Figure 5b). Additionally, slight particle collections were also observed in the Mg matrix, as shown in Figure 5c. These were expected since the number of added particles increased twofold.

Figure 6 displays SEM micrographs of the alloy refined with 1 wt% Al_2O_3. The secondary phase morphology and distribution were similar to the 0.25 and 0.5 wt% conditions. Specifically, the β-$Mg_{17}Al_{12}$ phase networks were refined and a slightly elongated flower-like morphology of the Mn–Al intermetallics was present. These effects were attributed to the refinement in grain size and the added Al_2O_3 particles. Alternatively, significant agglomeration of the Al_2O_3 particles was observed within the alloy microstructure, which is apparent in Figure 6b. Clusters of Al_2O_3 particles were observed near the β-phase, Mn–Al-based intermetallics and the Mg matrix. Such agglomerations can cause stress concentrations during tensile testing, which may lead to premature failure.

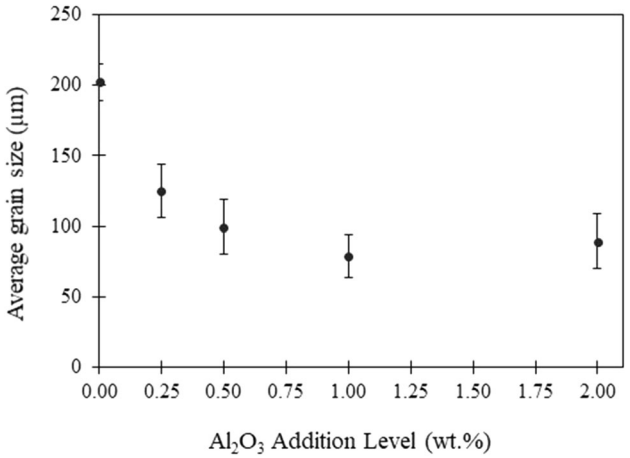

Figure 2. Average grain size of the base alloy and refined alloys as measured using the linear intercept procedure; error bars indicate one standard deviation about the sample mean.

Figure 7 displays SEM micrographs of the alloy refined with 2 wt% Al_2O_3. The alternate morphology of the Mn–Al-based phase was still present at this addition level (Figure 7b). As well, significant levels of Al_2O_3 particle agglomeration were observed in the alloy microstructure. Examples of the agglomeration are given in Figure 7a and c. It is evident that greater weight fractions of Al_2O_3 led to appreciable particle agglomeration. As observed in Figures 5 and 6, particle clustering was present at addition levels above 0.5 wt%. As a result, it can be concluded that the manual stirring process using an impeller is not effective in homogenously distributing grain refining particles above the 0.5 wt% threshold.

Mechanical Properties and Strengthening Mechanisms

The ultimate tensile strength, yield strength and % elongation (%EL) of the base alloy and the samples refined with Al_2O_3 were determined by tensile testing at ambient temperature. The results of the tensile tests are summarized in Figure 8. The UTS of the base alloy, in the as-cast condition without addition of Al_2O_3, was approximately 138 MPa (Figure 8a). With the addition of 0.25 wt% Al_2O_3, the UTS increased by 5% to 145 MPa. Further Al_2O_3 addition to 0.5 wt% increased the tensile strength to approximately 159 MPa. This marked an increase in tensile strength of nearly 15%. Increasing the Al_2O_3 particle content from 0.5 to 1 wt% did not further improve the UTS of the alloys. Similarly, no improvement in UTS was observed for the 2 wt% Al_2O_3 addition level. Therefore,

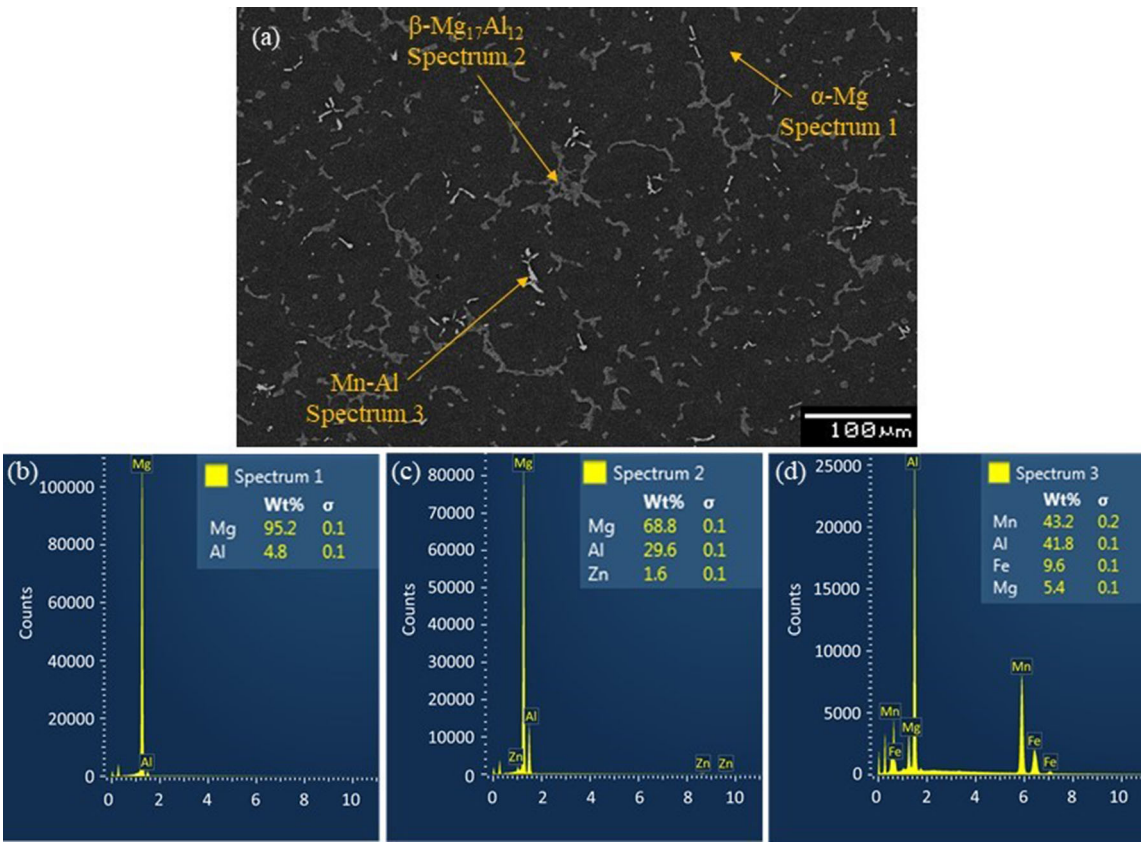

Figure 3. Scanning electron micrograph of (a) base alloy and corresponding EDS spectra of (b) Mg matrix, (c) β-$Mg_{17}Al_{12}$ phase and (d) Mn–Al phase.

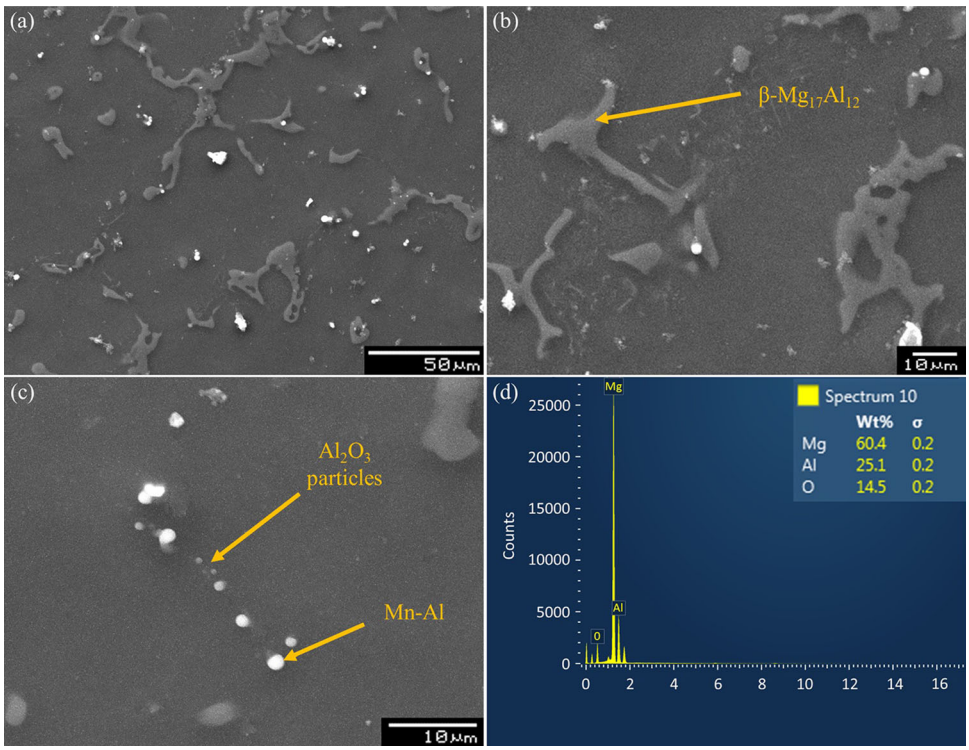

Figure 4. Scanning electron micrographs of the alloys refined with 0.25 wt% Al_2O_3 captured at (a) × 500 magnification, (b) × 1000 magnification, (c) × 1500 magnification and (d) EDS spectrum of Al_2O_3 particle.

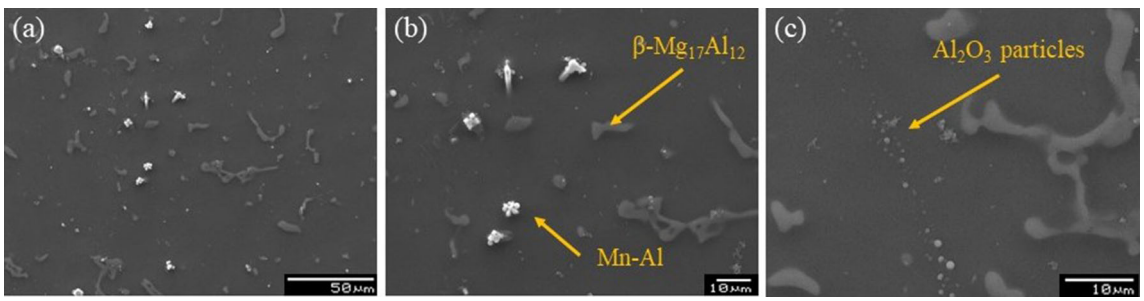

Figure 5. Scanning electron micrographs of the alloys refined with 0.5 wt% Al_2O_3 captured at (a) × 500 magnification, (b) × 1000 magnification and (c) × 1500 magnification.

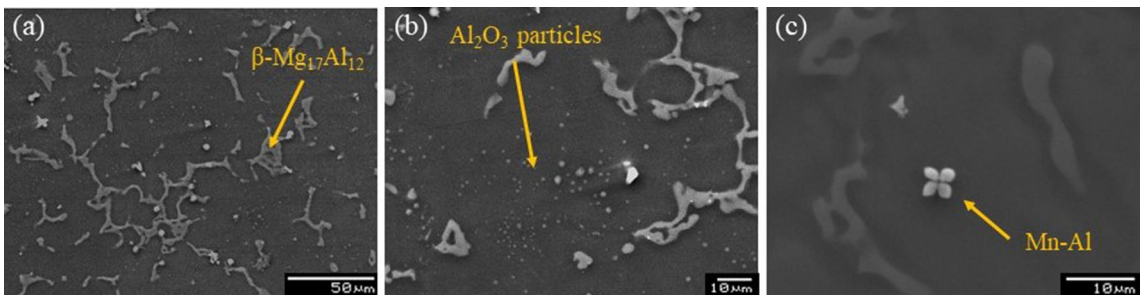

Figure 6. Scanning electron micrographs of the alloys refined with 1 wt% Al_2O_3 captured at (a) × 500 magnification, (b) × 1000 magnification and (c) × 1500 magnification.

particle additions above 0.5 wt% resulted in a negative effect on the UTS, such that at the 2 wt% Al_2O_3 addition level, the UTS was similar to the base alloy.

Figure 8b displays the ductility of the base alloy and the alloys refined with Al_2O_3 particles. The ductility of the samples displayed a similar trend when compared to the ultimate tensile strength. In the base condition, the ductility of the samples was approximately 1.4%. Upon adding 0.25 wt% Al_2O_3, the ductility increased to 1.6%. Moreover, further improvement in ductility was observed by increasing the Al_2O_3 content. At the 0.5 wt% addition level, the ductility increased to 2.5%. This is a significant improvement of approximately 79%. However, similar to the trend observed for UTS, increased Al_2O_3 particle addition above 0.5 wt% resulted in diminished alloy ductility. Upon adding 1 wt% and 2 wt% Al_2O_3, the ductility decreased to 1.6% and 1.3%, respectively. The highest of alloy ductility was achieved with the 0.5 wt% Al_2O_3 addition.

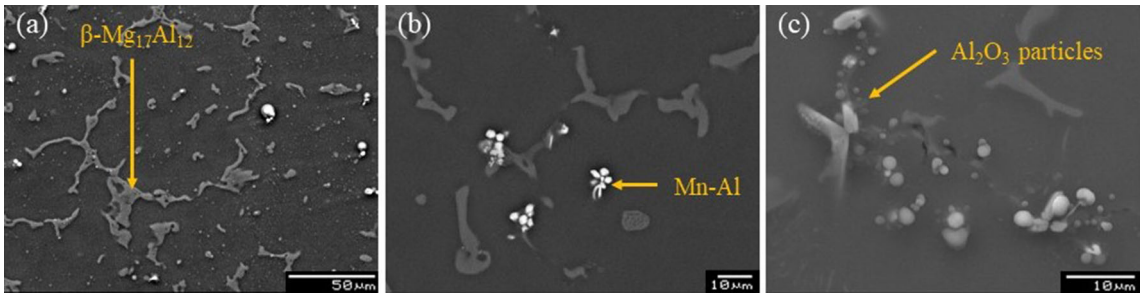

Figure 7. Scanning electron micrographs of the alloys refined with 2 wt% Al_2O_3 captured at (a) × 500 magnification, (b) × 1000 magnification and (c) × 1500 magnification.

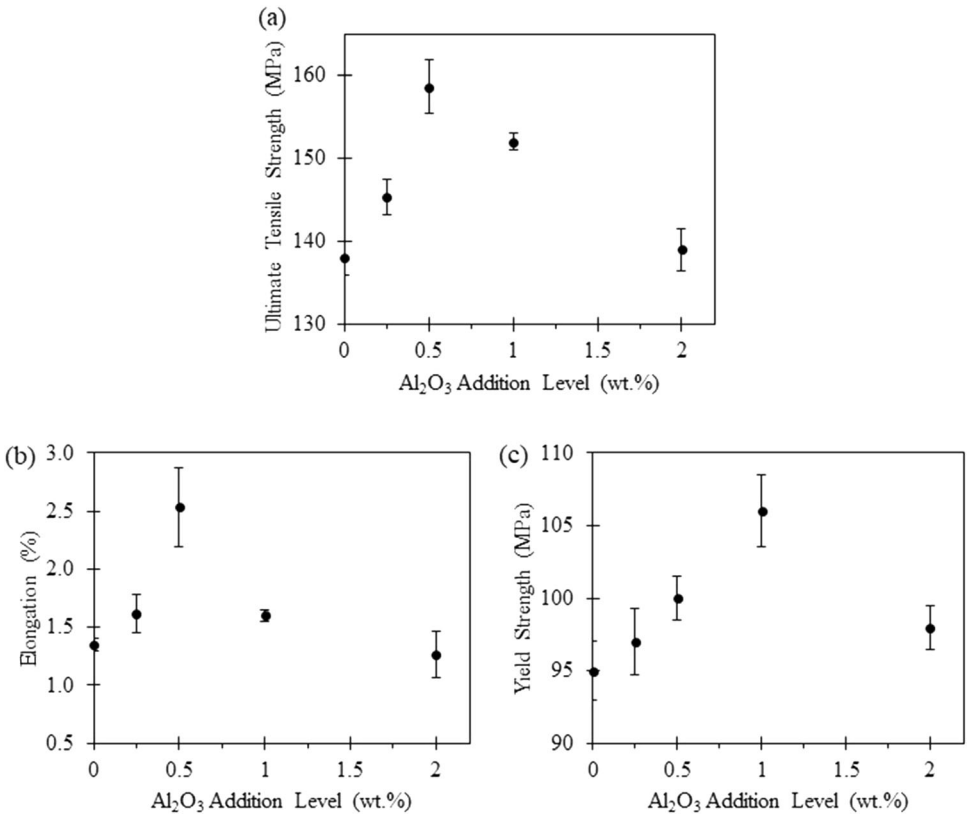

Figure 8. Mechanical properties of the AZ91E base alloy and the alloys refined with Al_2O_3 (a) ultimate tensile strength, (b) % elongation and (c) yield strength; error bars indicate one standard deviation about the sample mean.

The yield strength of the base and refined alloys is summarized in Figure 8c. The YS of the base alloy was measured to be approximately 95 MPa. With the addition of Al_2O_3, the YS of the alloys increased steadily up to 1 wt%, after which a decline was noticed. That is, with addition of 0.25 and 0.5 wt% Al_2O_3 particles, the YS increased to 97 MPa and 100 MPa, respectively. The highest measured YS was approximately 106 MPa, which was achieved by adding 1 wt% Al_2O_3. It must be noted that the trend observed for the YS differed from those of UTS and ductility where the maximum properties were achieved with the addition 0.5 wt% Al_2O_3. Increasing the refiner content to 2 wt% decreased the YS to 98 MPa, although slightly improved compared to the base alloy (95 MPa). The highest measured YS was seen for the 1 wt% Al_2O_3 particle addition level, with an increase in strength of approximately 12%.

To determine the mechanisms for the enhancement in YS of the alloys reinforced with Al_2O_3, a theoretical investigation of the strengthening mechanisms was conducted. Ceramic particle-reinforced alloys are typically strengthened through Hall–Petch strengthening, coefficient of thermal expansion strengthening and load transfer from particle to matrix. The Hall–Petch effects occur though the increase in grain boundary area, which is known to impede dislocation motion. Coefficient of thermal expansion strengthening occurs due to the mismatch of thermal expansion coefficients between the matrix and reinforcement particles. During solidification, the difference in CTE prompts the formation of geometrically necessary dislocations, which have been reported to hinder plastic deformation. The load-bearing effect of the particles operates on the principal that load can be transferred from the softer matrix (Mg) to the hard ceramic particle reinforcements (Al_2O_3). It is important to note that the Orowan strengthening mechanism was neglected in this study, since the added reinforcement particles were not nano-sized.[32]

The relative contribution of each of the above-mentioned mechanisms to the overall YS of the alloy can be determined using Eqn. 1.[33]

$$\Delta\sigma_{sum} = \Delta\sigma_{Hall-Petch} + \Delta\sigma_{CTE} + \Delta\sigma_{load} \quad \text{Eqn. 1}$$

where $\Delta\sigma_{Hall-Petch}$ is the increase in strength due to grain refinement, $\Delta\sigma_{CTE}$ is the increase in strength due the CTE mismatch, and $\Delta\sigma_{load}$ is the increase in strength due to load transfer from particle to matrix.

The incremental increase in strength due to the Hall–Petch phenomenon was estimated using Eqn. 2.[34,35]

$$\Delta\sigma_{Hall-Petch} = Kd_m^{-1/2} \quad \text{Eqn. 2}$$

where the Hall–Petch coefficient K is 0.13 MPa $m^{1/2}$[36] and d_m is the average grain size of the alloy.

The relative contribution of CTE mismatch strengthening to the overall strength of the alloy was calculated using Eqn. 3.[37]

$$\Delta\sigma_{CTE} = \sqrt{3}\beta G_m b\sqrt{\frac{12V_p\Delta\alpha\Delta T}{(1-V_p)bd_p}} \quad \text{Eqn. 3}$$

where the strengthening coefficient β is 1.25,[38] the shear modulus of the matrix G_m is 13.7 GPa, the magnitude of the burgers vector b is 0.2 nm,[39] the volume fraction of the added particles V_p was determined based on the refiner addition levels, the difference in thermal expansion coefficient between the particles and the matrix $\Delta\alpha$ is 17.6 $°C^{-1}$,[21,22] the difference in processing and test temperatures ΔT is 327 °C, and the average diameter of the added particles d_p is 1 μm.

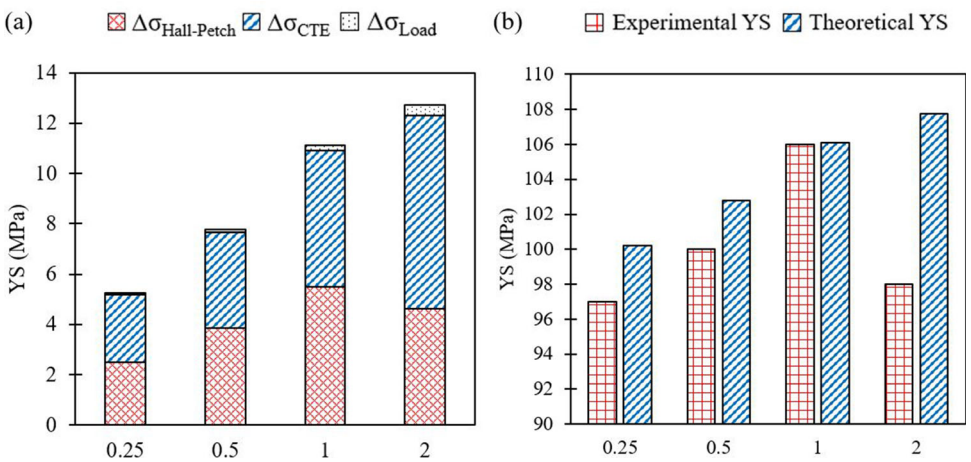

Figure 9. Incremental improvements in YS of the alloys refined with Al_2O_3, (a) theoretical improvements due to Hall–Petch, CTE mismatch and load-bearing mechanisms, (b) experimental to theoretical YS comparison.

Assuming round and equiaxed reinforcement particles, the incremental increase in strength due to the load transfer effect can be calculated using Eqn. 4.[40]

$$\Delta\sigma_{load} = 0.5\ V_p\sigma_0 \qquad \text{Eqn. 4}$$

where σ_0, the average YS of the unmodified alloy matrix is 95 MPa.

The relative contribution of each of the above strengthening mechanisms to the overall YS of the alloys was calculated based on Eqns. 1–4, and the results are displayed in Figure 9. Figure 9a displays a comparison of the effects of each individual strengthening mechanisms to the total YS of the alloys. It is clear that the Hall–Petch phenomenon has significant effect on the YS of the alloys. The enhancement in YS due to grain refinement increased with Al_2O_3 addition level up to 1 wt%, after which point it declined. This was expected since the average grain size of the alloys did not decrease after the 1 wt% Al_2O_3 addition level, and grain coarsening was observed thereafter. Further, CTE mismatch was also of significant importance to the overall YS of the alloys. With increasing Al_2O_3 particle content in the matrix, the theoretical improvements in YS due to CTE mismatch increased as well. The relative contribution to YS from CTE mismatch was comparable to the Hall–Petch effect up to the 1 wt% Al_2O_3 addition level, after which CTE mismatch became the dominant strengthening mechanism. Enhancement in YS due to the load-bearing effect appeared to be negligible in most cases. The greatest contribution was determined to be 0.4 MPa at the 2 wt% particle addition. In effect, it is suggested that the load-bearing mechanism could be wholly ignored in future analyses related to particle-reinforced Mg casting with the range in addition levels used in this study.

Figure 9b illustrates a comparison between experimentally measured and theoretically calculated YS of the reinforced alloys. Satisfactory correlation was observed between the theoretical and experimental YS results up to 1 wt% Al_2O_3 addition. However, it was observed that the theoretical models overestimated the YS for every instance. The largest discrepancy between the theoretical and experimental results was observed for the 2 wt% particle addition level. At this level, the theoretical mechanisms overestimated the YS by approximately 10 MPa. In addition, it must be noted that the experimentally obtained YS of the alloys displayed a sharp decline with the addition of 2 wt% Al_2O_3, as displayed in Figure 8. As a result, with the exception of the alloys reinforced with 2 wt% Al_2O_3, the theoretical strengthening mechanism contribution models displayed a similar trend when compared to the experimental results.

Discussion

With the addition of 1 μm α-Al_2O_3 particles, significant grain refinement was observed in the AZ91E Mg alloys. The highest level of refinement was observed for the 1 wt% Al_2O_3 addition level, which reduced the grain size approximately 61% relative to the base condition. The reduction in grain size was likely caused by increased nucleation of α-Mg from Al_2O_3 particle substrates. The presence of the particles in the microstructure near the Mn–Al phases and the center of grains suggested that they were stable in the melt and may have acted as substrates for heterogeneous nucleation. Moreover, the crystal structure of α-Al_2O_3 consists of an HCP sub-lattice, which suggested possible high crystallographic registry with HCP-Mg.[18] The density of Al_2O_3 (3.95 g/cm^3[19]) is higher than that of AZ91E (1.81 g/cm^3[25]), ensuring that the particles did not rapidly settle or float to the melt surface to be skimmed as dross. As a result, the significant level of grain refinement was likely brought about by heterogeneous nucleation from Al_2O_3 particle substrates.

Increasing the addition level of Al_2O_3 beyond 1 wt% did not result in further grain refinement. However, significant refinement relative to the base alloy was still present. The arrest in grain size reduction was likely caused by particle agglomeration. As observed in Figure 7a and c, the considerable number of added particles for the 2 wt% Al_2O_3 addition level led to appreciable agglomeration, leaving fewer particles available to participate in the nucleation of Mg. The previous research has established that beyond a specific threshold of nucleant addition, grain refinement no longer occurs, leading to grain coarsening and detriments to mechanical properties.[41] Therefore, the 1 wt% Al_2O_3 addition level was determined to be the threshold for effective grain refinement. Increasing the refiner particle content from 1 to 2 wt% did not further improve the grain size.

Microstructural observation revealed that the alloy secondary phases were influenced by the Al_2O_3 particle addition. Notably, with increasing Al_2O_3 content, the β-$Mg_{17}Al_{12}$ phase became more refined. In particular, the average size of the phase appeared to be smaller, and the networks-like structure became shorter. As was discussed previously, the β-phase primarily precipitated on grain boundaries. Moreover, since the grain size of the alloys decreased with Al_2O_3 addition, it followed that the β-phase became more refined. This is due to the increased grain boundary area, which allowed the β-phase to precipitate in more areas throughout the microstructure, leading to overall morphological refinement. As a result, the refinement in the β-$Mg_{17}Al_{12}$ phase was determined to be a side effect of grain refinement using Al_2O_3 particles.

In addition to the β-phase, the Mn–Al intermetallics were also affected by Al_2O_3 particle addition. With addition of Al_2O_3 between 0.5 and 2 wt%, an alternative flower-like morphology of the Mn–Al phase was observed. This result is demonstrated in Figures 5b, 6c and 7b. Upon close examination, it appeared that in each instance of the

alternate shape, the Mn–Al intermetallics were surrounded by Al_2O_3 particles. Effectively, the particles seemed to hinder the growth of the Mn–Al phase in particular directions, leading to a flower-like morphology. It should be recalled that the alternate shape of the Mn–Al phase was not observed in either the base alloy or the alloy refined with 0.25 wt% Al_2O_3. This may have been due to the significantly fewer number of particles available in the melt and their more homogenous distribution in the solidified alloy matrix.

As previously mentioned, the distribution of the Al_2O_3 particles in the matrix was homogenous up to the 0.25 wt% addition level. Minimal signs of particle agglomeration were observed with the addition of 0.5 wt% Al_2O_3. Further, at 1 and 2 wt% Al_2O_3, significant signs of agglomeration and clustering were seen in the microstructure. Ceramic particle agglomeration is a common side effect observed in stir cast particle-reinforced castings. With larger particle addition levels, the overall number of particles rises. As a result, the frequency of inter-particle collisions increases, leading to their eventual coalescence and agglomeration.[41] Also, particles can spontaneously agglomerate with one another to reduce their surface energies. These effects are more pronounced with decreasing particle size, and especially high for nanoparticles. In most cases, for micron-sized particles, as used in this study, manual stirring with an impeller is adequate to break up particle clusters. However, longer stirring time or higher rpm must be utilized to achieve such results. In either case, since Mg has a high affinity for oxygen, vigorous and lengthy stirring times often lead to entrapped oxides in the final castings, which result in reduced mechanical properties. As a result, one must carefully weigh the benefits and drawbacks of increased particle additions, stirring time and rpm as well as potential lack of melt cleanliness.

The mechanical properties of the alloys were also improved as a result of Al_2O_3 addition. Specifically, the UTS of the refined castings showed signs of enhancement up to additions of 0.5 wt% Al_2O_3. Thereafter, the tensile strength declined. With increasing Al_2O_3 particle addition, the microstructure and grain size of the alloys become more refined. Most notably, the refinement in the β-$Mg_{17}Al_{12}$ secondary phase was critical, since it is known to be brittle and precipitates along grain boundaries. It is likely that these effects led to the enhancement in tensile strength of the particle-reinforced alloys. However, as stated previously, significant particle agglomeration was observed with addition levels beyond 0.5 wt% Al_2O_3. Ceramic particle agglomeration is well known to cause stress concentrations, which can lead to premature failure during tensile testing. As a result, the 1 and 2 wt% Al_2O_3 addition levels displayed significantly lower UTS as compared to 0.5 wt% addition.

The ductility of the samples displayed a similar trend to UTS. In particular, the elongation to failure of the castings improved up to 0.5 wt% Al_2O_3 addition. With addition levels beyond 0.5 wt%, a steady decline in ductility was observed. In effect, the elongation to failure of the castings refined with 2 wt% Al_2O_3 was comparable to that of the base alloy. The enhancement in ductility likely occurred through the same mechanisms that were stated above for tensile strength. To reiterate, the overall homogenization of the grain structure and secondary phases alleviated the stress concentrations in the alloy microstructure. Conversely, the elongation to failure of the castings with 1 and 2 wt% Al_2O_3 was compromised due to the agglomeration of Al_2O_3 particles in the matrix. Therefore, Al_2O_3 addition was effective in enhancing the ductility of the cast alloys up to 0.5 wt%.

The YS of the refined alloys did not behave in an analogous manner as UTS and ductility. Specifically, the yield stress displayed signs of enhancement up to 1 wt% addition of Al_2O_3, whereas UTS and ductility improved only up to 0.5 wt% addition. This outcome likely occurred since, as described in the previous section, YS is highly dependent on grain size and CTE mismatch between the particles and the matrix. In fact, with increasing particle content, the relative contribution of the strengthening mechanisms was shown to increase. However, since the grain size did not improve beyond 1 wt% Al_2O_3, incremental increase in YS due to the Hall–Petch effect also did not increase, albeit theoretical improvements due to CTE mismatch were still increasing. As a result, the arrest in grain size at 1 wt% Al_2O_3 addition coupled with the significant refiner particle agglomeration likely led to the decline in YS at the 2 wt% Al_2O_3 addition level as opposed to 1 wt%.

An attempt was made to use theoretical models to predict the YS of the refined alloys. Moreover, the theoretical YS contributions of the Hall–Petch effect, CTE mismatch between the added particles and the alloy matrix and load-bearing capacity were determined. It must be emphasized that the load-bearing capacity of the particles was deemed to be inconsequential toward the overall YS, and hence, their further analysis was neglected by the authors. The theoretical results displayed good correlation with the experimental findings for 0.25. 0.5, and 1 wt% additions, as demonstrated by the relatively low deviations of 3.3%, 2.8% and 0.1%, respectively. However, such was not the case for the 2 wt% Al_2O_3 addition level, since the theoretical models overpredicted the YS by approximately 10 MPa (9.9% deviation). The authors believe the overestimation of the YS was due to the inability of the CTE mismatch strengthening model to account for elevated levels of particle agglomeration in the alloy matrix. Effectively, the CTE mismatch model continued to predict higher values for YS even when the particles were clustered. Such was not the case for the grain boundary strengthening effect. As mentioned previously, the grain

size did not decrease after 1 wt% Al_2O_3 addition. Consequently, the Hall–Petch equation did not continually predict an increase in YS beyond 1 wt% particle addition. It is clear that the overprediction in YS was solely caused by the CTE mismatch model, which was determined to be a drawback in its application to particle-reinforced castings.

In summary, it was shown that reinforcement with 1 μm Al_2O_3 particles up to 0.5 wt% was effective in decreasing the grain size, refining the secondary phases and improving the overall mechanical properties of cast AZ91E Mg alloys. These results were significant, since they were achieved using conventional casting methods currently utilized in industry, such as permanent mold casting and mechanical stirring with an impeller. Furthermore, Al_2O_3 is inexpensive and abundant, which are both crucial qualities for industrial application. As a result, Al_2O_3 addition was able to provide a simple and effective means for improving the properties of Mg alloys for use in consumer electronics, aerospace applications and the transportation sector.

Further research is required to fully examine the relationship between AZ91E Mg alloy and Al_2O_3 particle addition. For example, the effects of a range of particle sizes in the micron-scale regime could be examined, as well as the effects of varying holding times, stirring times and stirring rpm. Additionally, it was observed that the inability of the CTE mismatch strengthening model to account for inter-particle spacing was a significant drawback in its application to particle-reinforced castings. Consequently, efforts could be expended toward alleviating the shortcomings of the model by incorporating an inter-particle spacing parameter, such as that of the Orowan strengthening model.

Conclusions

In this study, the effects of grain refinement using 1 μm α-Al_2O_3 particles on the microstructure and mechanical properties of AZ91E Mg alloy were investigated. Cast samples were evaluated with respect to grain size, secondary phase morphology and mechanical properties. In addition, theoretical strengthening mechanism models were used to determine the incremental contribution of grain boundary strengthening, CTE mismatch strengthening and particle load-bearing capacity to the overall strength of the alloy. The results from this research enabled a unique understanding of the effects of varying Al_2O_3 addition level on the secondary phase characteristics and mechanical properties of AZ91E.

The following conclusions can be drawn from this work:

1. The addition of Al_2O_3 up to 1 wt% resulted in a decrease in grain size relative to the base alloy. Further addition beyond 1 wt% did not improve the alloy grain size. The grain refinement was likely caused by heterogeneous nucleation of α-Mg from Al_2O_3 particle substrates.
2. The morphology of the β-$Mg_{17}Al_{12}$ phase was enhanced through Al_2O_3 addition. It is suggested that this was caused by the overall increase in grain boundary area due to grain refinement.
3. Mechanical stirring was effective in distributing the Al_2O_3 particles up to 0.5 wt%. Further additions resulted in particle clustering and agglomeration which were deemed to be detrimental to mechanical properties.
4. The mechanical properties of the alloy were also improved through the addition of Al_2O_3. This was attributed to a combination of grain boundary strengthening, CTE mismatch strengthening and the overall homogenization of the alloy microstructure.
5. The strengthening mechanism models were indeed effective in predicting the YS of the refined alloys. However, shortcomings were identified in incorporating the effects of inter-particle spacing for the CTE mismatch model.

Acknowledgements

The first two authors gratefully acknowledge the support of the Natural Sciences and Engineering Research Council (NSERC) for the award of Canada Graduate Scholarships (CGSD3 - 535728 – 2019 and CGSD3 - 559982 - 2021). The authors would also like to thank the members of the Centre for Near-net-shape Processing of Materials, Mr. Alan Machin, Mr. Michael Rinaldi and Mr. Adam Belcastro, for their support with this research.

Funding

This work was supported by Natural Sciences and Engineering Research Council of Canada (Grant Numbers CGSD3 - 535728 - 2019 and RGPIN-06096).

REFERENCES

1. A. Luo, Recent magnesium alloy development for elevated temperature applications. Int. Mater. Rev. **49**, 13–30 (2004)
2. E. Emley, *Principles of Magnesium Technology* (Pergamon Press, Oxford, 1966)
3. H. Tsukamoto, Enhancement of mechanical properties of SiCw/SiCp-reinforced magnesium composites fabricated by spark plasma sintering. Results Mater. **9**, 100167 (2021)
4. D.Z. Shamami, S.M. Rabiee, M. Shakeri, Use of rapid microwave sintering technique for the processing of magnesium–hydroxyapatite composites. Ceram. Int. **47**, 13023–13034 (2021)

5. M.M. Castro, P.H.R. Pereira, A. Isaac, R.B. Figueiredo, Development of a magnesium–alumina composite through cold consolidation of machining chips by high-pressure torsion. J. Alloys Compd. **780**, 422–427 (2019)
6. M. Shen, X. Wang, H. Li, M. Zhang, T. Ying, K. Nie, K. Wu, Effects of (micron + submicron + nano) multisized SiC particles on microstructure and mechanical properties of magnesium matrix composites. J. Compos. Mater. **52**, 2055–2064 (2018)
7. X. Pi, W. Yu, C. Ma, X. Wang, S. Xiong, A. Guitton, Materials (2020). https://doi.org/10.3390/ma13040995
8. R.V. Vignesh, R. Padmanaban, M. Govindaraju, Synthesis and characterization of magnesium alloy surface composite (AZ91D–SiO_2) by friction stir processing for bioimplants. SILICON **12**, 1085–1102 (2020)
9. H. Mohammadi, M. Emamy, Z. Hamnabard, The statistical analysis of tensile and compression properties of the as-cast AZ91-X%B_4C composites. Inter. Metalcast. **14**, 505–517 (2020)
10. S. Saha, C. Ravindran, Grain refinement of AZ91E and Mg-9 wt.% Al binary alloys using zinc oxide. Inter. Metalcast. **9**, 33–42 (2015). https://doi.org/10.1007/BF03355600
11. P. Emadi, E. Vandersluis, C. Ravindran, Prediction and verification of effective grain refiners for magnesium alloys. Trans. Indian Inst. Met. **71**, 2771–2775 (2018)
12. Z. Ma, C. Li, J. Du, M. Zhan, Grain refinement of Mg–Al alloys inoculated by MgO powder. Inter. Metalcast. **13**, 674–685 (2019)
13. S. Ganguly, S. Sarkar, A.K. Mondal, Mater. Int. (2020). https://doi.org/10.1007/s12540-020-00744-3
14. F. Aydin, Y. Sun, M.E. Turan, The effect of TiB_2 content on wear and mechanical behavior of AZ91 magnesium matrix composites produced by powder metallurgy. Powder Metall. Met. Ceram. **57**, 564–572 (2019)
15. K. Nie, Z. Zhu, P. Munroe, K. Deng, Y. Guo, Microstructure and mechanical properties of TiC nanoparticle-reinforced Mg−Zn−Ca matrix nanocomposites processed by combining multidirectional forging and extrusion. Trans. Nonferrous Met. Soc. China **30**, 2394–2412 (2020)
16. A. Azad, L. Bichler, A. Elsayed, Effect of a novel Al–SiC grain refiner on the microstructure and properties of AZ91E magnesium alloy. Inter. Metalcast. **7**, 49–59 (2013). https://doi.org/10.1007/BF03355564
17. W.H. Gitzen, *Alumina as a Ceramic Material* (The American Ceramic Society, Columbus, 1970)
18. W.E. Lee, P.D. Lagerlof, Structural and electron diffraction data for sapphire (α-Al_2O_3). J. Electron. Microsc. Tech. **2**, 247–258 (1985)
19. E. Dorre, H. Hubner, *Alumina-Processing Properties and Applications* (Springer, Berlin, 1984)
20. I. Levin, D. Brandon, Metastable alumina polymorphs: crystal structures and transition sequences. J. Am. Ceram. Soc. **81**, 1995–2012 (1998)
21. W. Zhu, J. Chen, C. Hao, J. Zhang, Microstructure and strength of Al_2O_3/Al_2O_3 joints bonded with ZnO–Al_2O_3–B_2O_3–SiO_2 glass–ceramic. J. Mater. Sci. Technol. **30**, 944–948 (2014)
22. H. Dieringa, Properties of magnesium alloys reinforced with nanoparticles and carbon nanotubes: a review. J. Mater. Sci. **46**, 289–306 (2011)
23. L. Kovarik, M. Bowden, J. Szanyi, High temperature transition aluminas in δ-Al_2O_3/θ-Al_2O_3 stability range: review. J. Catal. **393**, 357–368 (2021)
24. M. Qian, D. StJohn, M. Frost, Heterogeneous nuclei size in magnesium–zirconium alloys. Scr. Mater. **50**, 1115–1119 (2004)
25. M. Avedesian, H. Baker, *Magnesium and Magnesium Alloys* (ASM International, Materials Park, 1999)
26. *Standard Specification for Aluminum-Alloy Permanent Mold Castings*, ASTM B108-06 (2006)
27. *Standard Test Methods for Tension Testing Wrought and Cast Aluminum- and Magnesium-Alloy Products*, ASTM B557-15 (2015)
28. *Standard Practice for Heat Treatment of Magnesium Alloys*, ASTM B661-12 (2012)
29. *Standard Test Methods for Determining Average Grain Size*, ASTM E112-13 (2013)
30. T. Chen, X. Jiang, H. Huang, Y. Ma, Y. Li, Y. Hao, Semisolid microstructure of AZ91D magnesium alloy refined by $MgCO_3$. Inter. Metalcast. **6**, 43–54 (2012)
31. A. Zhang, H. Hao, X. Zhang, Grain refinement mechanism of Al–5C master alloy in AZ31 magnesium alloy. Trans. Nonferrous Met. Soc. China **23**, 3167–3172 (2013)
32. W. Miller, F. Humphreys, Strengthening mechanisms in particulate metal matrix composites. Scr. Metall. **8**, 25–33 (1991)
33. A. Sanaty-Zadeh, Comparison between current models for the strength of particulate-reinforced metal matrix nanocomposites with emphasis on consideration of Hall–Petch effect. Mater. Sci. Eng. A **531**, 112–118 (2012)
34. E.O. Hall, The deformation and ageing of mild steel: III discussion of results. Proc. Phys. Soc. **64**, 747–755 (1951)
35. N.J. Petch, The cleavage strength of polycrystals. J. Iron Steel Inst. **174**, 25–28 (1953)
36. P. Xiao, Y. Gao, C. Yang, Z. Liu, Y. Li, F. Xu, Microstructure, mechanical properties and strengthening mechanisms of Mg matrix composites reinforced with in situ nanosized TiB_2 particles. Mater. Sci. Eng. A **710**, 251–259 (2018)
37. R. Arsenault, N. Shi, Dislocation generation due to differences between the coefficients of thermal expansion. Mater. Sci. Eng. **81**, 175–187 (1986)
38. K. Nie, K. Deng, X. Wang, K. Wu, Characterization and strengthening mechanism of SiC nanoparticles

reinforced magnesium matrix composite fabricated by ultrasonic vibration assisted squeeze casting. J. Mater. Res. **32**, 2609–2620 (2017)
39. C. Caceres, C. Davidson, J. Griffiths, C. Newton, Effects of solidification rate and ageing on the microstructure and mechanical properties of AZ91 alloy. Mater. Sci. Eng. A **325**, 344–355 (2002)
40. V. Nardone, K. Prewo, On the strength of discontinuous silicon carbide reinforced aluminum composites. Scr. Metall. **20**, 43–48 (1986)
41. C. Ti-jun, W. Rui-quan, H. Hai-jun, M. Ying, H. Yuan, Grain refining technique of AM60B magnesium alloy by $MgCO_3$. Trans. Nonferrous Met. Soc. China **22**, 1533–1539 (2012)